AGU PUBLICATIONS

JGR

Journal of Geophysical Research: Space Physics

RESEARCH ARTICLE
10.1002/2014JA020664

Key Points:
- The main mechanism of the PRE is the curl-free response to the *F* region dynamo
- The seasonal variations of the PRE results from all three mechanisms
- The different mechanisms produce different PRE altitude profiles

Correspondence to:
J. V. Eccles,
vince.eccles@spacenv.com

Citation:
Eccles, J. V., J. P. St. Maurice, and R. W. Schunk (2015), Mechanisms underlying the prereversal enhancement of the vertical plasma drift in the low-latitude ionosphere, *J. Geophys. Res. Space Physics*, *120*, 4950–4970, doi:10.1002/2014JA020664.

Received 30 SEP 2014
Accepted 28 APR 2015
Accepted article online 30 APR 2015
Published online 1 JUN 2015

Mechanisms underlying the prereversal enhancement of the vertical plasma drift in the low-latitude ionosphere

J. V. Eccles[1], J. P. St. Maurice[2], and R. W. Schunk[3]

[1]Space Environment Corporation, Providence, Utah, USA, [2]Institute for Space and Atmospheric Studies, University of Saskatchewan, Saskatoon, Saskatchewan, Canada, [3]Center for Atmospheric and Space Science, Utah State University, Logan, Utah, USA

Abstract The evening prereversal enhancement (PRE) of the vertical plasma drift has important consequences for the Appleton density anomaly and the stability of the nighttime ionosphere. Simplified simulations were used to review the three competing theories of the PRE origin, to explore their relative importance, and to indentify their interdependence. The mechanisms involved in the generation and climatology of the PRE are, first, a curl-free electric field response to rapid changes in the vertical electric field associated with the nighttime *F* region dynamo; second, a divergence of Hall currents in the *E* region away from the magnetic equator; and, third, the moderating effect of the large Cowling conductivities in the equatorial *E* region. The simulations indicate that the equatorial Cowling conductivity creates an important current path that limits the other two mechanisms prior to equatorial sunset and releases them after equatorial sunset. The curl-free mechanism is the dominant mechanism when the terminator and magnetic meridian are aligned in part due to the accelerating *F* region zonal wind. When the solar terminator is not aligned with the magnetic meridian, there is an interaction involving all three mechanisms contributing to the magnitude and timing of the PRE. Finally, the altitude profile of the PRE decays more quickly with altitude when the curl-free mechanism dominates as compared to when the Hall current mechanism dominates.

1. Introduction

In the evening low-latitude ionosphere, there are deterministic and turbulent plasma structures, both of which depend on the magnitude of the zonal electric field and accompanying vertical $\mathbf{E}\times\mathbf{B}$ plasma drift. The quiet time electrodynamics in the low-latitude ionosphere is a complex system that is normally examined through a separation of its various components (e.g., equatorial electrojet, solar quiet current, prereversal enhancement, and evening plasma vortex). However, each part is related to the others within the ionosphere-thermosphere-electrodynamic system. This paper focuses on the physics of the prereversal enhancement (PRE) of the equatorial zonal electric field near local sunset and indulges in a review of low-latitude electrodynamics to provide context for the discussion on the cause of the PRE.

Early studies of the low-latitude electrodynamics have focused on the slight deflections of ground-based magnetometer measurements generated by ionospheric electric fields and neutral winds driving currents in the highly conductive *E* layer (100 to 120 km) [*Baker and Martyn*, 1953; *Stening*, 1969; *Tarpley*, 1970a, 1970b; *Richmond et al*., 1976]. Modeling of conductivities, electric fields, and currents is simplified using the assumption that magnetic field lines are approximately constant electric potentials. This is true in the case of perpendicular electric fields of scale sizes larger than 10 km [*Farley*, 1959]. This permits the 3-D electrodynamics to be solved using a 2-D electric potential equation at some preferred 2-D coordinate surface of the geophysical environment. One 2-D representation can be obtained by integrating currents and conductivities vertically in altitude to represent a thin-shell conductivity layer. A second 2-D representation integrates currents and conductivities along magnetic field lines and represents the electrodynamics at the plane of the magnetic dip equator [*Haerendel*, 1973; *Singh and Cole*, 1987a, 1987b, 1987c; *Haerendel et al*., 1992; *Eccles et al*., 2004]. The 3-D electric field can be reconstructed from the 2-D solution using equations defining the dipole magnetic field line geometry (see Appendix A of *Haerendel et al*. [1992]). The early studies of ionospheric electric fields assumed that the *E* layer (100 to 150 km local altitude) dominates the conductivities and ionospheric currents driven by neutral wind tides to produce the average solar quiet current system [e.g., *Tarpley*, 1970b]. The tidal winds of the *E* region altitudes are

well represented by Hough function modes described by *Forbes and Lindzen* [1976]. Gradients in the neutral wind-driven currents and *E* region conductivities would generate polarization electric fields, causing ionospheric plasma to drift primarily in the direction of the *E* region tidal neutral winds. These polarization electric fields in the low-latitude ionosphere cause plasma near the magnetic dip equator to rise during the day under an eastward zonal component of the electric field and descend during the night.

The daily thermal variations due to solar heating of the thermosphere drive neutral winds in the *F* region ionosphere. *Rishbeth* [1971a, 1971b, 1973] proposed that the small local conductivities of the *F* region in comparison to *E* region conductivities could not be ignored in the low-latitude ionosphere due to the large horizontal distances of the magnetic field lines in the equatorial *F* region. The very long horizontal orientation of the magnetic field through the equatorial *F* region provides significant integrated Pedersen conductance when compared to the integrated *E* region Pedersen conductance at the feet of those same field lines. The *F* region neutral wind dynamo currents have limited effect on daytime electric fields when *E* region conductance is large compared to the integrated *F* region conductance. However, the *E* region conductance decays quickly after sunset, while the *F* region decays slowly through the night. This permits the *F* region neutral wind dynamo to generate large vertical electric fields during the night. *Heelis et al.* [1974] produced a global electrodynamic model that included the *F* region dynamo by modeling parallel currents into and out of the *E* layer conductivity model of *Tarpley* [1970a, 1970b]. The main result of the *F* region dynamo is to generate large downward electric fields in the equatorial *F* region, causing the *F* region plasma to drift 80 to 130 m/s eastward after sunset in the direction of the neutral wind.

Near sunset, a regular feature in the eastward electric field (upward plasma drift) appears just prior to the electric field reversal to the west (downward plasma drift). This prereversal enhancement (PRE) can lift the *F* region plasma profile 100 to 200 km above its typical altitude. The magnitude of the PRE has been correlated with the dramatic plasma irregularity development of the evening equatorial ionosphere [*Fejer et al*., 1999]. While the PRE varies with solar condition, season, and longitude [*Scherliess and Fejer*, 1999], it also exhibits night-to-night variability that currently defies prediction.

This paper describes and examines the theories of the PRE: the first by *Rishbeth* [1973] and *Eccles* [1998a], the second by *Farley et al.* [1986] (the first paper to focus on the PRE cause), and finally by *Haerendel and Eccles* [1992]. *Eccles* [1998b] previously reviewed the theories of the PRE origin, but the conclusions were ambiguous. We therefore examine PRE using simplified situations in a field line-integrated electric field model to clarify these mechanisms and their influence on the PRE magnitude. We clarify the fundamental differences between the mechanism suggested by *Rishbeth* [1971b] and *Eccles* [1998a] (curl-free mechanism or CFM) and the mechanism discussed in *Farley et al.* [1986] (Hall current divergence mechanism or HCDM). The role of the equatorial *E* region with high Cowling conductivity in the development of the PRE [*Haerendel and Eccles*, 1992] is also examined in relation to the CFM and HCDM. We introduce the models used in the study in section 2. Section 3 presents the theories of the PRE origin. Section 4 provides a simplified modeling demonstration of each theory based on equinox conditions and then examines differences during solstice conditions. Section 5 discusses and summarizes the results of simulations of the PRE.

2. Field Line-Integrated Electrodynamic Model

To model the low-latitude ionospheric electric fields, we have coupled the Ionosphere Forecast Model of *Schunk et al.* [1997] with the middle- and low-latitude electrodynamic models of *Eccles* [2004]. These two models have been designed to couple with any thermosphere model whether empirical or physics based. For this study we use the NRLMSISE-00 atmosphere model [*Picone et al*., 2002] for neutral densities and temperatures. We construct a neutral wind description adequate for our electrodynamic study (described below).

The Ionosphere Forecast Model (IFM) is a physics-based numerical model of the global ionosphere. The model calculates 3-D, time-dependent density distributions for four major ions (NO^+, O^+, N_2^+, and O_2^+) at *E* region altitudes, two major (O^+ and NO^+), and two minor (N_2^+ and O_2^+) ions at *F* region altitudes. The IFM also contains a simple prescription for calculating H^+ densities in the *F* region and topside ionosphere. The IFM ion and electron temperatures in the low and middle latitudes are provided by the Titheridge temperature model [*Titheridge*, 1998]. For this study, we use 2° latitude resolution, 5° longitude resolution, and a variable altitude grid from 94 km to 1600 km.

For ionospheric electric fields, we assume, first, that current divergence is equal to zero and, second, magnetic field lines are infinite conductors. The electrostatic 3-D current equation can be integrated into a 2-D current continuity equation, which becomes a potential equation with current dynamo gradients as source terms. Our field line-integrated current model is described in *Haerendel et al.* [1992] and *Eccles* [2004]. The magnetic field lines are mathematically treated as dipole field lines, but geographic location of the field lines is generated by field line tracing of the International Geomagnetic Reference Field [*Finley et al.*, 2010]. The fundamental electrodynamic quantities of the model are field line integrations of Pedersen and Hall conductivities and conductivity-weighted integrations of local neutral winds along the field line in a local coordinate frame of a dipole magnetic field with the parallel component, ℓ; zonal perpendicular component, s; and meridional perpendicular component, q,

$$\Sigma_P = R_E L \int \sigma_P \left(1 + 3\zeta^2\right) d\zeta \tag{1a}$$

$$\Sigma_P = R_E L \int \sigma_P d\zeta \tag{1b}$$

$$U_L^P = \frac{R_E L}{\Sigma_P} \int \sigma_P u_q \frac{\left(1 + 3\zeta^2\right)}{\left(1 - \zeta^2\right)^{\frac{3}{2}}} d\zeta \tag{1c}$$

$$U_\varphi^P = \frac{R_E L}{\Sigma_P} \int \sigma_P u_s \frac{\left(1 + 3\zeta^2\right)^{\frac{1}{2}}}{\left(1 - \zeta^2\right)^{\frac{3}{2}}} d\zeta \tag{1d}$$

$$\Sigma_H = R_E L \int \sigma_H \left(1 + 3\zeta^2\right) d\zeta \tag{1e}$$

$$U_L^H = \frac{R_E L}{\Sigma_H} \int \sigma_H u_q \frac{\left(1 + 3\zeta^2\right)}{\left(1 - \zeta^2\right)^{\frac{3}{2}}} d\zeta \tag{1f}$$

$$U_\varphi^H = \frac{R_E L}{\Sigma_H} \int \sigma_H u_s \frac{\left(1 + 3\zeta^2\right)^{\frac{1}{2}}}{\left(1 - \zeta^2\right)^{\frac{3}{2}}} d\zeta \tag{1g}$$

These equations define the field line-integrated Pedersen conductivity, Σ_P; the field line-integrated Pedersen conductivity with different field line metrics, $\widetilde{\Sigma}_P$; the Pedersen-weighted zonal neutral wind, $U_\varphi{}^P$; and the Pedersen-weighted meridional neutral wind, $U_L{}^P$, and field line-integrated Hall conductivity, Σ_H; the Hall-weighted zonal neutral wind, $U_\varphi{}^H$; and the Hall-weighted meridional neutral wind, $U_L{}^H$. R_E is the Earth's radius, L is the radial variable in the magnetic dip equator plane measured in Earth radii, and $\zeta = \sin\lambda$ (λ is the dipole latitude). Within the integrals are the local conductivities, σ_P and σ_H, and the local winds, u_s and u_q. The s is perpendicular to **B**, that is, only horizontal and zonal. The q is the perpendicular component that is vertical and meridional. The limits of integration begin in the southern hemisphere below the E region, where parallel currents are zero and end in the northern hemisphere below the northern E region.

The above definitions are determined by the integration of the 3-D local current continuity equation along field lines into a 2-D current continuity equation in polar coordinates (φ and L),

$$\frac{1}{R_E L}\left(\frac{\partial(LJ_L)}{\partial L} + \frac{\partial J_\varphi}{\partial_\varphi}\right) = 0 \tag{2}$$

where the field line-integrated current densities are

$$J_L = \Sigma_P \left(E_L + B(L) U_\varphi^P\right) - \Sigma_H \left(E_\varphi - B(L) U_L^H\right) \tag{3a}$$

$$J_\varphi = \widetilde{\Sigma}_P \left(E_\varphi - B(L) U_L^P\right) + \Sigma_H \left(E_L + B(L) U_\varphi^H\right) \tag{3b}$$

E_L and E_φ are the vertical and zonal electric field components at the field line apex, and $B(L)$ is the magnitude of the magnetic field at the apex altitude. For this study, we ignore gravitational current and pressure-term currents contained in the *Eccles*'s [2004] model since the PRE does not arise from these currents terms, although *Eccles* [2004] does demonstrate that the gravity-driven currents do modify the PRE magnitude slightly. The solution plane is the magnetic dip equatorial plane.

Figure 1 plots the geometry of the field line-integrated solar quiet (Sq) and equatorial electrojet (EEJ) current system. While the electrodynamics has been reduced to a 2-D model by assuming equipotential field lines, a

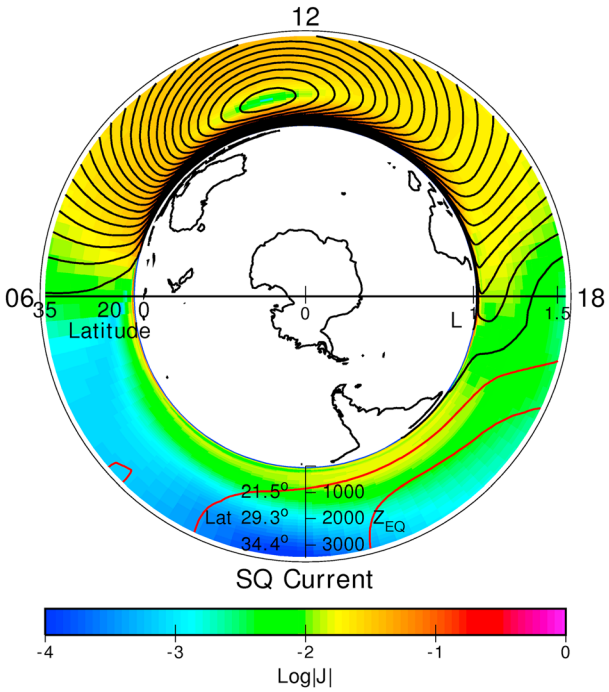

Figure 1. Field line-integrated ionospheric electrodynamic quantities in the apex coordinate plane. Current magnitude (color scale of log value), current flow lines with black lines for counterclockwise flow and red lines for clockwise flow. The left side *x* axis shows the value of the magnetic latitude of a dipole field line foot in the north and south *E* regions. The right side radius axis is measured in Earth radii.

3-D electric field and current system can be reconstructed from this 2-D model using formulae presented in the Appendix A of *Haerendel et al.* [1992].

In our investigation, we divide the field line integrals into *E* and *F* region portions with 150 km as the dividing altitude. The potential equation and electric fields are obtained using the whole field line-integrated ionosphere, but we can examine the *E* and *F* region neutral wind drivers and the *E* and *F* region currents by dividing the integrals prior after the whole field line solution. The field line integration can also be divided by hemisphere with northern and southern *E* region portions of the integrals to examine their importance within the whole field line solution. Thus,

$$\Sigma_P = \Sigma_P^E + \Sigma_P^{ES} + \Sigma_P^{EN} \tag{4a}$$

$$\Sigma_H = \Sigma_H^F + \Sigma_H^{ES} + \Sigma_H^{EN} \tag{4b}$$

$$U_\varphi^P = \frac{\Sigma_P^F U_\varphi^{PF} + \Sigma_P^{ES} U_\varphi^{PES} + \Sigma_P^{EN} U_\varphi^{PEN}}{\Sigma_P^F + \Sigma_P^{ES} + \Sigma_P^{EN}} \tag{4c}$$

$$U_L^P = \frac{\Sigma_P^F U_L^{PF} + \Sigma_P^{PES} U_L^{PES} + \Sigma_P^{EN} U_L^{PEN}}{\Sigma_P^F + \Sigma_P^{PES} + \Sigma_P^{EN}} \tag{4d}$$

where *F*, *ES*, and *EN* indices designate *F* region, southern hemisphere *E* region, and northern hemisphere *E* region partial integrations. The respective apex altitude profiles and totals are plotted in Figure 2. For the equatorial electrodynamics, one can assume that $\widetilde{\Sigma}_P = \Sigma_P$ in equation (3b). Because the *F* region contains only a small amount of Hall conductivity, the Hall conductivity-weighted neutral winds are essentially limited to the *E* region portion of the integration. For field lines with an apex altitude below 150 km, there is obviously no *F* region component in the integration of Hall currents. These field lines (<150 km apex altitude) represent the region of the equatorial electrojet (EEJ). The EEJ is associated with the strong eastward ionospheric currents near noon at the magnetic dip equator due to the Cowling effect. In the electrodynamic model, the integrated Cowling conductivity is given by

$$\Sigma_C = \widetilde{\Sigma}_P + \frac{\Sigma_H^2}{\Sigma_P}$$

[*Haerendel and Eccles*, 1992]. We use EEJ to refer to the equatorial ionosphere where the Cowling effect is strongest; that is, the apex altitude ranges from 100 km to 150 km (Figure 2). This altitude region remains a dominant current channel throughout all local daytime hours.

The coupled IFM-electrodynamic model has been used to successfully simulate real conditions of the equatorial ionosphere [*Eccles et al.*, 2011]. Other low-latitude ionosphere electric field models based on highly conductive field lines [*Huba et al.*, 2008; *Richmond and Fang*, 2015] contain the same essential physics and should produce very similar PRE magnitudes and shapes given the same neutral atmosphere, neutral wind, and ionosphere conditions. The infinitely conducting field lines assumption degrades the solution in comparison to a more rigorous modeling with using finite parallel conductivities. The simplification tends to include too much influence from the Hall conductivity in the off-equator ionosphere. This systematic error is estimated to provide an average uncertainty of 10% or less in the following results.

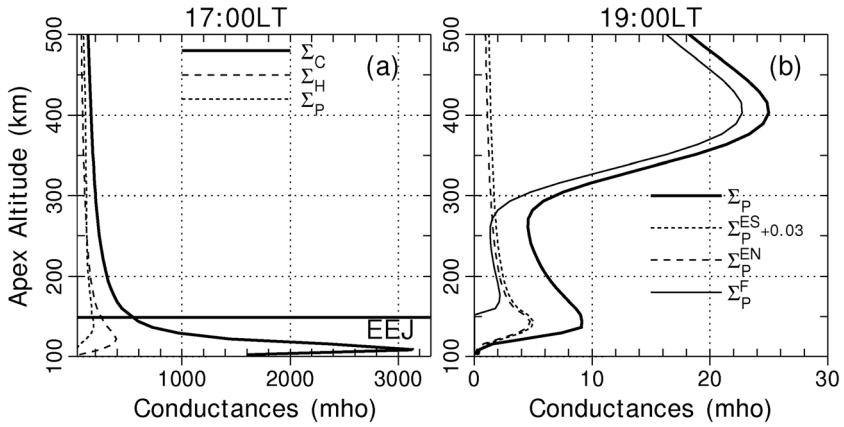

Figure 2. (a) Total field line-integrated conductances of Pedersen (short dash), Hall (long dash), and Cowling (solid line) at 17:00 LT. (b) Pedersen conductance (thick solid line) with partial field line integrations through the *F* region (thin solid line), the northern *E* region (long dash), and the southern *E* region (short dash) at 19:00 LT.

3. Prereversal Enhancement Review

At sunset, the eastward electric field and the resulting **E** × **B** vertical plasma drift are frequently enhanced (prereversal enhancement or PRE), lifting the ionosphere 100 or more kilometers before the electric field turns westward and the plasma drift downward for the rest of the night. The rising ionosphere is partly responsible for the unstable conditions associated with the explosive plasma irregularities in the evening equatorial ionosphere called equatorial spread *F* [*Haerendel*, 1973; *Woodman and La Hoz*, 1976, and others]. In the complex 3-D electrodynamics of the equatorial ionosphere, the precise cause of the PRE is quite difficult to identify using global models. There is general agreement that the *F* region dynamo provides the free energy of the electrodynamic system for generating the PRE lift of the ionosphere.

The potential causes of the PRE are discussed in (1) *Rishbeth* [1973] and *Eccles* [1998a], (2) *Farley et al.* [1986], and (3) *Haerendel and Eccles* [1992]. All three PRE causes are examined here using field line-integrated electrodynamics but with simplified conditions to clarify the relationships and relative importance of each mechanism. *Farley et al.* [1986] use a height-integrated *E* layer model of electrodynamics in their description of the PRE. Both field line- and height-integrated *E* region models are valid in the examination of off-equator physics, but the field line-integrated model provides a clearer insight into the PRE mechanism proposed by *Farley et al.* due to the difficulty of the height-integrated models in handling the horizontal field line configuration of equatorial electrodynamics. The following subsections strive to diagram and describe the basic physics of the mechanisms.

3.1. The Edge of the Nighttime *F* Region Dynamo (Curl-Free Mechanism)

Rishbeth [1971a, 1971b] proposed that the long magnetic field lines through the equatorial *F* region would allow the *F* region neutral wind current dynamo to generate strong downward polarization electric fields during the night when *E* region conductances were low. Figure 3 diagrams the winds, currents, electric fields, and plasma drifts for the dayside, sunset, and nightside conditions. The *F* region and the *E* regions of both hemispheres are presented as planes with gray scale indicating field line-integrated magnitudes of the Pedersen conductivity in each region. Late in the afternoon, the *F* region zonal neutral wind (U_φ, blue arrows) turns eastward and generally continues eastward until morning. The neutral wind in the *F* region generates vertical Pedersen current (yellow arrows with black outline to indicate dynamo current) in the integrated *F* region. The divergence of this vertical dynamo current occurs at the bottom and top of the *F* region dynamo. We use plus-minus sign to indicate regions of current divergence within the current continuity model. The field lines of the current divergences are also the field lines where charging would occur in a time-dependent, 3-D current model with negative charge accumulating on the field lines intersecting the bottom of the *F* region dynamo and a more diffuse region of positive charge at the top or polarward extent of the dynamo. The downward polarization electric field (black arrows) arising

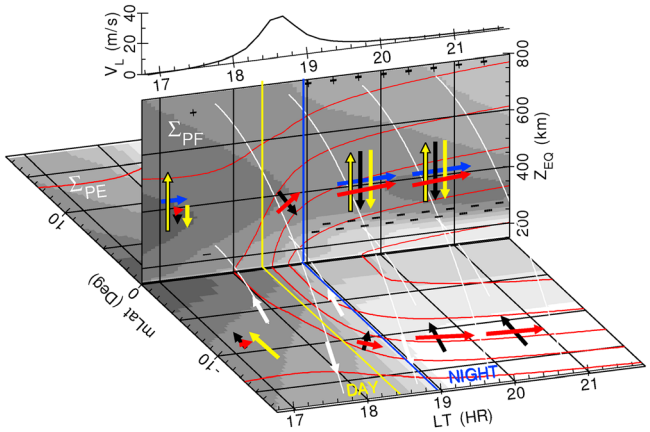

Figure 3. Schematic of the curl-free mechanism. The zonal *F* region neutral wind (blue arrows) moves through the field line-integrated *F* region (vertical plane at dip equator) and drives a vertical dynamo current (thin yellow arrows with black outlines). Current divergences occur at the bottom and top of the field line-integrated *F* region (negative and positive signs) creating electric fields (black arrows). The *F* region is coupled to the off-equator *E* region where daytime Pedersen currents (yellow arrows) short out the *F* region dynamo electric fields with field-aligned currents (white arrows) connecting the *E* and *F* regions. After sunset, the small *E* region conductance permits larger downward electric fields causing the plasma to drift (red arrows) with the neutral wind. The rapid change of the downward electric fields at *E* region sunset produces a small horizontal electric field as an edge effect and the PRE vertical drift (top plot). The flow lines of plasma flux tubes ($\mathbf{E} \times \mathbf{B}$ drift) are plotted with red potential contours.

between the bottom and topside dynamo current divergences causes the *F* region plasma to drift in the eastward direction (red arrows) with the neutral wind. The integrated *F* region connects with the off-equator *E* region through parallel currents (white arrows) into and out of the integrated *E* region.

During the daytime, the *E* region's high conductance along with the *F* region conductance provides a significant equatorward and downward currents $((\Sigma_P{}^F + \Sigma_P{}^E)E_L)$ (yellow arrows with no black outline) to balance the upward *F* region dynamo current. The large daytime *E* region conductance reduces the magnitude of the electric field required to balance the vertical dynamo current in the *F* region; thus, the daytime zonal plasma drift is small.

At sunset, the *E* region decays quickly to very low nighttime levels, while the integrated *F* region conductance remains large. The *F* region wind dynamo current is no longer shorted out by the field line-connected *E* region conductance. Thus, a large downward polarization electric field develops. Most of the Pedersen return current needed to balance the *F* region dynamo current is provided by the *F* region itself $(\Sigma_P{}^F E_L)$. The strong downward polarization electric field in the *F* region causes the plasma to drift at near the neutral wind speed until morning [*Chapagain et al.*, 2013]. The downward polarization electric field rapidly increases at *E* region sunset to approximately 3 V/m for an ~120 m/s eastward plasma drift speed prior to midnight. *Rishbeth* [1971b] stated in a single sentence that the sharp sunset edge of this *F* region dynamo polarization electric field produces an edge effect and a small zonal component to the electric field in the *F* region corresponding to a vertical drift. A small westward electric field is predicted in the integrated *F* region topside. However, the accumulation of positive charge at the top (outer meridional extent) of the *F* region dynamo is spread over a much broader region than the bottomside negative charge, so the sunset edge effect in the *F* region topside will be much smaller. This does predict an altitude-dependent PRE generated by the CFM.

The model of *Heelis et al.* [1974] produced the dominant *F* region dynamo downward polarization field during the nighttime and produced the PRE of the eastward electric field near-sunset terminator. However, the importance of the PRE and the cause of the PRE were not the focus of their studies, and the *F* region dynamo edge effect as the cause of the PRE was not presented again until *Eccles* [1998a, 1998b]. *Eccles* [1998a] used the curl freeness of the rapidly changing vertical electric field at sunset to demonstrate that the PRE magnitude is proportional to the zonal gradient of the downward polarization electric field generated by the *F* region dynamo. The top line graph of Figure 3 shows the upward PRE associated with the CFM as a sunset edge effect from simulations with only the *F* region zonal wind as the active dynamo driver.

We recapitulate *Eccles* [1998a] to demonstrate the reasonableness of the curl-free mechanism (CFM) as a cause of the PRE, but we will demonstrate later that this is not the whole story of the CFM. The first assumption in *Eccles* [1998a] is that the field line-integrated electrodynamics of the low-latitude ionosphere is dominated by the vertical gradients. For simplicity, we will move to Cartesian coordinates, $R_E L\varphi$ to x and $R_E(L-1)$ to z, since the altitude region of the important physics is much smaller than the

radius of the Earth. In this field line-integrated system, z is the field line apex altitude. Under the assumption that the vertical gradients dominate low-latitude electrodynamics, equation (2) becomes

$$\frac{\partial J_z}{\partial z} \approx 0 \tag{5}$$

Equations (3a) and (5) can be reduced to

$$J_z(150\ \text{km}) = \Sigma_P B\left(\frac{E_z}{B} + U_x^P\right) - \Sigma_H B\left(\frac{E_x}{B} + U_z^H\right) \tag{6}$$

where J_z(150 km) is the *Sq* current moving down into or up out of the EEJ. Near sunset, this current is drawn up through the field line-integrated conductivity as approximately a constant value. The *E* region meridional winds are near zero around the hours of sunset; thus, $U_z{}^H = 0$. The plasma drifts are given by

$$V_x = -\frac{E_z}{B} \tag{7a}$$

$$V_z = \frac{E_x}{B} \tag{7b}$$

inserting equation (7) into equation (6) and solving for V_x

$$V_x = U_x^P - \frac{\Sigma_H}{\Sigma_P} V_z - \frac{J_z(150\ \text{km})}{B\Sigma_P} \tag{8}$$

This is the zonal plasma drift formula described in *Haerendel et al.* [1992], which contains the physics of the shear in the zonal plasma drift near sunset. $U_x{}^P$ is a combination of both the *E* and *F* region conductivity-weighted neutral winds (equation (4c)). Just after sunset, the integrated Pedersen conductivity has a strong altitude dependence, which accentuates the affect of the upward current from the electrojet region (J_z term). The J_z term enhances the zonal drift shear below the integrated *F* region as described in *Haerendel et al.* [1992]. This formula works well through the altitudes of the equatorial *F* region (150 km $< z <$ 1000 km). The last two terms of equation (8) only modify the zonal drift at altitudes on and below the *F* region bottomside, where the *F* region Pedersen conductivity is still small [*Haerendel et al.*, 1992]. For the apex altitudes near the integrated *F* peak, equation (8) can be further simplified to

$$V_x(t) = U_x^P(t) \tag{9}$$

as in *Eccles* [1998a]. This simple description of the zonal plasma drift is appropriate near and above the *F* region peak at all local times. Near sunset, the zonal neutral wind in the *E* region is near zero, thus using equation (4c)

$$V_x(t) \approx U_x^P = U_x^{PF}\left(\frac{\Sigma_P^F}{\Sigma_P^E + \Sigma_P^F}\right) \tag{10}$$

This formula captures the *F* region dynamo theory of *Rishbeth* [1971a, 1971b] for the zonal plasma drift around sunset. Prior to sunset, the *E* region conductance causes the $\mathbf{E}\times\mathbf{B}$ drift to be smaller than the *F* region neutral wind. After sunset, when the *E* region conductance becomes very small, the plasma $\mathbf{E}\times\mathbf{B}$ drifts almost exactly with the *F* region neutral wind.

Equation (10) can now be used to examine the PRE as a curl-free ($\nabla \times E = 0$) effect of the *F* region dynamo. The important term of the curl of the electric field is

$$\frac{\partial E_z}{\partial x} - \frac{\partial E_x}{dz} = 0 \tag{11}$$

For the Sun-synchronous physics of the PRE, $x = -v_T t$, where v_T is the speed of the terminator (485 m/s) at the *F* region bottomside altitude of 300 km. Dividing by the magnetic field magnitude at 300 km, which only varies slowly with apex altitude, we can pose it in terms of plasma drifts

$$\frac{\partial V_{\text{PRE}}(z)}{\partial z} = -\frac{\partial V_x(t)}{\partial t} \tag{12}$$

The zonal plasma drift in equation (12) can be replaced by the conductivity-weighted zonal neutral wind, $U_x^P(t)$ (equation (10)). This zonal wind peaks near the *F* region peak (~400 km) and remains approximately constant

up to 1000 km [*Fejer et al.*, 1985]. There is a shear in the conductivity-weighted zonal wind near the *F* region bottomside and the associated shear in the zonal plasma drift [*Haerendel et al.*, 1992]. The *F* region dynamo operates above the shear up to the altitude extent of the Appleton anomaly (~1000 km or higher). The PRE plasma drift is strongest near the *F* region bottomside and goes to zero by around 800 km or 900 km depending on the solar conditions (see Figure 6 in *Eccles et al.* [1999]). We can approximate this altitude decay of the PRE vertical plasma drift with a linear equation maximizing at 300 km (V_{PRE}) and going to zero at 900 km. These altitudes, 300 to 900 km, are the approximate altitudes of the curl-free relationship between the PRE and the rapid change in the downward polarization electric field of the nighttime *F* region dynamo. We can explore the relationship by integrating both sides of equation (12) through this altitude region. Using equations (9) and (12) with the characteristics of the PRE vertical drift and the zonal drift, one gets

$$\int_{300\ \mathrm{km}}^{900\ \mathrm{km}} \left[V_{\mathrm{PRE}}(t, 300\ \mathrm{km}) \frac{(900 - z)}{600} \right] dz \approx - \int_{300\ \mathrm{km}}^{900\ \mathrm{km}} \frac{1}{v_T} \frac{\partial U_x^P(t)}{\partial t} dz \tag{13}$$

The time variation on the *F* region zonal plasma drift near sunset generates a vertical drift due to the zonal neutral wind accelerating into the nightside and the *E* region conductivity decaying. Estimating the average PRE magnitude by

$$V_{\mathrm{PRE}}(t) = \frac{60000\ \mathrm{m}}{485\ \mathrm{m/s}} \frac{\partial U_x^P(t)}{\partial t} \tag{14}$$

If we assume an *F* region zonal drift acceleration of ~100 m/s per hour near sunset for equinox conditions, one gets an average PRE magnitude of about 25–30 m/s for the sunset period. The timing of the PRE maximum value is synchronized with the *E* region sunset at around 18:40 LT in the above example (Figure 3, top). This time-dependent 1-D analysis suggests that the PRE magnitude from the CFM is proportional to the time rate of change in the conductivity-weighted *F* region neutral wind dynamo near sunset. We note that the CFM does not generate the downward turn in the vertical drift after the PRE that is observed in the data. Instead, the CFM must depend on the nighttime downward drifts imposed by *E* region tides for the nighttime downward drift.

3.2. Hall Current Divergence Mechanism in the Off-Equator *E* Regions

Farley et al. [1986] was the first paper to focus on the PRE cause. They used an *E-F* region current continuity model similar to *Heelis et al.* [1974]. The simulation experiment used a constant eastward *F* region wind of 200 m/s and with all *E* region winds and *F* region meridional winds set to zero. They concluded that a large eastward zonal *F* region wind across the solar terminator was all that is necessary to produce the PRE. The *F* region vertical dynamo currents generated the downward polarization electric fields in the *F* region causing the nighttime zonal plasma drift as predicted by the *F* region dynamo theory of *Rishbeth* [1971b], and a large vertical plasma drift (PRE) resulted at the sunset solar terminator. The constant *F* region eastward wind of 200 m/s across the sunset terminator provided a causal link to the PRE within the numerical model. The authors identified the important current gradients to be in the Hall conductivity of the off-equator *E* region at sunset and tied to the bottomside of the *F* region dynamo. We refer the reader to examine their explanation based on their height-integrated conductivity model [*Farley et al.*, 1986].

We now explain the Hall current divergence mechanism (HCDM) of *Farley et al.* [1986] using field line-integrated electrodynamics rather than the height-integrated *E* conductivity model. The HCDM begins with the *F* region dynamo generation of large downward electric field produced by the nighttime *F* region dynamo. The HCDM mechanism is a separate influence on the PRE magnitude and shape. It resides directly in the Hall currents driven by the downward (equatorward) polarization electric fields produced by the *F* region dynamo in both the daytime and nighttime (Figure 4). The eastward *F* region dynamo creates downward polarization electric fields. The nighttime electric field magnitude is twice as large as the daytime field for the case of the constant eastward neutral wind at sunset, because the combined *F* and *E* region Pedersen conductivity is approximately halved at sunset. However, the daytime Hall conductivity is approximately 20 times the nighttime conductivity. The downward electric fields drive a westward Hall current (green arrows), but this current is approximately 10 times larger during the daytime as at night. Thus, the negative divergence of westward Hall current, $\Sigma_H E_L$, across the solar terminator has a secondary

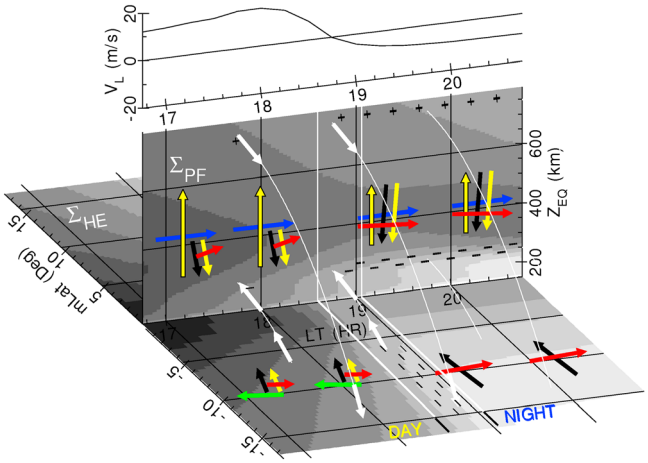

Figure 4. Schematic of the Hall current divergence mechanism. The *F* region zonal neutral wind (blue arrows) produces the dynamo currents (narrow yellow arrows with black outlines). The divergences of the dynamo current are the source terms (negative and positive signs) on the *F* region bottomside and topside, which produce mostly downward directed polarization electric fields (black arrows). The daytime *E* region provides significant balancing currents (yellow arrows) and reduces the electric fields. However, the daytime downward electric fields produce westward Hall currents (green arrows) prior to sunset, which are reduced to near zero after sunset. Negative Hall current divergence is generated at the solar terminator creating a small eastward electric field prior to sunset (the PRE) and a westward field after sunset (associated vertical drift in the top plot).

consequence due to the main downward polarization electric fields associated with the *F* region dynamo electrodynamics. Since the zonal *F* region dynamo wind is the primary generator of the PRE, we can ignore the meridional wind and the *E* region zonal wind for the sunset period for equation (3b). This gives the balancing terms for the HCDM:

$$J_\varphi = \Sigma_P E_\varphi + \Sigma_H E_L \qquad (15)$$

The negative divergence in zonal Hall current (second term on the RHS of equation (15)) near the solar terminator in the off-equator *E* region is an electric field source term at the sunset terminator. This generates an eastward electric field just prior to *E* region sunset (upward plasma drift in the *F* region) and a westward electric field just after *E* region sunset (downward plasma drift). The field line-integrated Hall conductance decreases with increasing apex altitude so the HCDM effect will be stronger at lower altitudes. The shear vertical electric field, which occurs after sunset, intensifies the HCDM effect at the shear altitude since the *F* region neutral wind dynamo is operating at these altitudes prior to sunset in the F_1 region. *Farley et al.* [1986] identified the largest current divergence in the off-equator *E* region tied by field lines to the *F* region bottomside.

It should be noticed that the variation of the zonal electric field and vertical plasma drift produced by the HCDM may have timing issues with the observed peak of the PRE. The HCDM produces a PRE peak on the dayside of *E* region sunset (near 18:00 LT in Figure 4, top). However, the mechanism does generate the oft-observed steep downward turn in the vertical drift after the PRE peak.

3.3. The Role of the EEJ on the PRE

Haerendel and Eccles [1992] recognized the multidimensional aspects underlying the PRE cause by describing the role the equatorial electrojet (EEJ) in determining the PRE magnitude. The Cowling conductance effect at the magnetic dip equator makes the EEJ a main pathway of current closure for the daytime *E* region dynamo observed as the *Sq*-EEJ current system. This is evident in the high density of current flow lines in the EEJ in Figure 1. The description of the role of the EEJ on the PRE magnitude depends on the field line-integrated electrodynamic model described in section 1. Our schematic in Figure 5 does not separate the *E* and *F* region components of the field line integration as displayed in Figures 3 and 4. *Haerendel and Eccles* [1992] agrees with *Farley et al.* [1986] and *Eccles* [1998a] that the ultimate cause of the PRE is associated with the *F* region zonal neutral wind dynamo near the sunset terminator. The upward *F* region dynamo current can be considered as slowly varying in local time (or longitude) when compared with the rapid sunset of the off-equator *E* regions. During the nighttime, the vertical polarization electric field generated by the *F* region dynamo currents drives a balancing downward current in the altitudes of the large *F* region conductivity. When there are no changes in the *F* region dynamo and underlying conductivities, then there is no net vertical current. Near sunset, both the *E* region conductivities and the *F* region neutral wind dynamo are changing, and the rapid changes create an unbalanced current in the direction of the *F* region dynamo current (upward). This net (unbalanced) vertical current is the current paradigm equivalent to an edge effect of the electrical charge paradigm of *Rishbeth* [1971b] and *Eccles* [1998b].

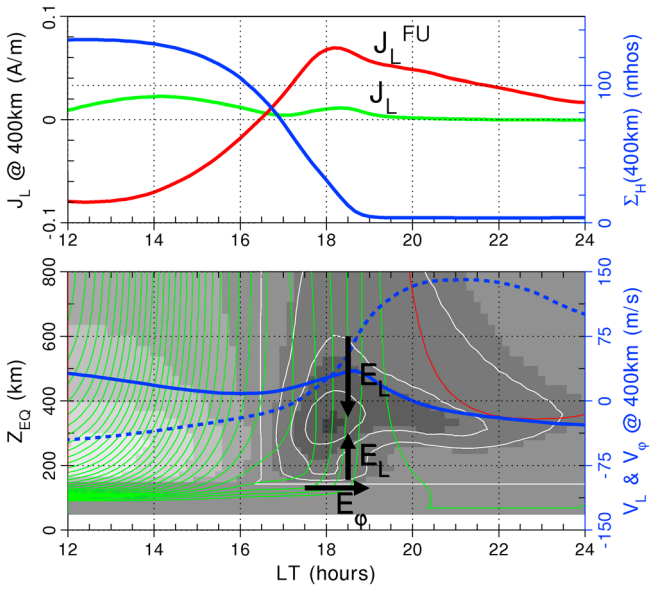

Figure 5. Schematic of the EEJ role in the PRE magnitude. The gray scale contour plot is of the integrated *F* region vertical current density with upward flow indicated by the white contour lines. The current flow lines indicate flow direction (green is counterclockwise and red clockwise), and the density of the flow lines indicates magnitude of the flow. The zonal (dashed blue lines) and vertical (solid blue lines) plasma drifts are plotted in the bottom plot with the right-hand axis showing magnitude. The decrease in Hall conductivity at 400 km is plotted to indicate sunset (top plot, blue line). The net vertical current density, J_L, increases near sunset (top plot, green line). The *F* region dynamo current, J_L^{FU}, is plotted in the top graph (red line). The PRE zonal electric field (E_φ) is enhanced to draw horizontal EEJ current toward the end of the sunset period. The EEJ current divergence is then drawn up to feed the net *F* region dynamo current by an enhanced vertical electric field below the *F* region (E_L from 150 to 250 km).

The net upward current through the field line-integrated ionosphere is indicated by the green current flow lines in (Figure 5). Flow line density is proportional to the current density magnitude. However, we caution that our stretched vertical altitude scale compared to horizontal spatial scale distorts the relationship between the horizontal and vertical densities of current flow lines in Figure 5. The contour lines indicate current flow direction with green contours flowing counterclockwise and red contours flowing clockwise. The density of the near-vertical current flow lines in Figure 5 (bottom) indicates that the net vertical current decreases to a local minimum around 17:00 LT and increases near sunset at 18:00 LT to 18:45 LT. The total vertical current density is plotted in Figure 5 (top) for $Z_{EQ} = 300$ km (green line). The timing of the unbalanced net current correlates with the rapid changes in the off-equator *E* region conductivity (apex altitude above 150 km). The magnitude of the driven *F* region dynamo current (red) is also plotted in Figure 5 (top). After 20:00 LT, the vertical dynamo current is nearly in perfect balance with the electric field-driven Pedersen current for near-zero vertical current. The net upward current in the *F* region around sunset requires current from below within the current continuity model. This current is best supplied by the upward divergences of horizontal current in the highly conductive path of the EEJ. The EEJ horizontal current is drawn toward and through the sunset period by an elevated PRE zonal electric field, which is then diverted upward into the *F* region by an upward electric field below the *F* region bottomside as described in *Haerendel et al*. [1992]. The increased upward electric field between the EEJ and the *F* region enhances a shear in the vertical electric field at the *F* region bottomside [*Haerendel et al*., 1992]. The PRE and the shear in the vertical electric field produce the observed plasma drift vortex structure [*Tsunoda et al*., 1981; *Kudeki et al*., 1981; *Eccles et al*., 1999]. *Haerendel and Eccles* [1992] state that PRE magnitude increases due to the need to draw horizontal current from the dayside EEJ to feed the bottom of the net (unbalanced) *F* region dynamo current. The EEJ conductivity becomes the regulating load and the determiner of the PRE magnitude in response to the *F* region dynamo electromotive force. Additionally, they indicate that the vertical drift of the PRE reduces the EEJ conductance by lifting ionization out of the EEJ altitudes to further increase the PRE magnitude.

The concepts of *Haerendel and Eccles* [1992] have been revisited by *Prakash et al.* [2009]. They include the return currents from the evening *F* region dynamo to the dayside *Sq* current system at the outer extension of the equatorial ionization anomaly, which limits the PRE to the equatorial ionosphere. For this paper, we treat these two papers as a single theory of current closure through the EEJ as the dominant regulator of the PRE magnitude.

4. Simplified Model Studies of the PRE Cause

We move from schematic descriptions to simplified simulations to elucidate the proposed mechanisms of the PRE. For these simplified simulations, we use realistic ionosphere and thermosphere parameters for medium-high solar conditions ($F_{10.7} = 150$) and low geomagnetic conditions ($Kp = 1$). The ionosphere conditions are solved by using the coupled IFM and global electrodynamic model. The thermosphere density is based on NRL-MSIS2000e [*Picone et al.*, 2002]. Thermospheric winds are generated by a combination of a solar diurnal tide and a solar semidiurnal tide in the *E* region, and horizontal wind model 2007 winds for the *F* region [*Drob et al.*, 2008], but with a different *F* region zonal wind near the dip equator (±5°) designed to reproduce the climatological zonal plasma drifts of *Fejer et al.* [1985, 2005] in the electrodynamic results. The field line-integrated electrodynamic model [*Eccles*, 2004] calculates conductivities and conductivity-weighted neutral winds from the 3-D ionosphere and thermosphere. The model solves the field line-integrated potential equation using an accelerated nine-point successive overrelaxation method on a grid with 2.0° longitude resolution and variable altitude resolution. The numerical solution of the equations for each ionosphere-atmosphere condition is accurate to within 98% of the steady state solution for the convergence criteria for the iterative numerical method.

For these studies, we run a full day simulation of the coupled ionosphere-electrodynamic results to obtain realistic ionosphere profiles on day with a typical PRE magnitude of 30 m/s at the peak. These results compare favorably with both zonal and vertical plasma drifts of *Scherliess and Fejer* [1998, 1999]. We then produce a simplified sunset condition to study the PRE mechanisms; this includes removing the *E* region tides and the meridional *F* region winds because it can be demonstrated within the coupled model that the PRE is generated by the zonal *F* region wind dynamo during quiet conditions. First, we use the apex altitude profiles of the field line-integrated conductivities from 17:00 LT for all local times and generate the LT dependence of magnitudes with a multiplicative factor. The total field line-integrated profiles of Hall and Pedersen conductivities at 17:00 LT from 50 km to 2000 km are broken into partial field line integrations (equation (4)) as discussed in section 2. Thus, there are three partial field line integrations at 17:00 LT profile for the *F* region (Σ_F^P), the northern *E* region (Σ_{EN}^P), and the southern *E* region (Σ_{ES}^P). We produce nighttime values of *E* region conductivities between 18:00 LT and 06:00 LT by dividing the daytime *E* region conductance profiles by 20, which approximates the day-night difference in the profiles of 17:00 LT and 19:00 LT. For these first simplified simulations, the 18:00 LT is a node in the numerical method and always has the average of the day and night profiles for a twilight condition. The *F* region conductivities are the same for day and night. This approximates the slow decay of the *F* region conductance across the sunset terminator.

Charge accumulation does occur on field lines involved in cross-field current gradients. We identify the regions of current gradient source terms on equipotential field lines using a 2-D Poisson's equation in the perpendicular directions at the dip equator plane. The 2-D Poisson's equation for the field line-integrated model is

$$\frac{1}{R_E L}\left(\Lambda(L)\frac{\partial LE}{\partial L} + \mathrm{M}(L)\frac{\partial E_\varphi}{\partial \varphi}\right) = \frac{Q}{\varepsilon_o} \tag{16}$$

where $\Lambda(L)$ and $\mathrm{M}(L)$ are the geometric factors associated with the charge distribution along dipole field lines. The equation assumes a highly conductive field line to distribute the charge along each field line such that $E_l = 0$. See the Appendix A for derivation of equation (6).

4.1. Comparing the Curl-Free Mechanism and Hall Current Divergence Mechanism

For the first four studies, the EEJ region (apex altitudes below 150 km) will have only nighttime profiles at all local times to remove the EEJ influence on the PRE. Figure 6 presents these four cases of low-latitude electrodynamics to reveal the characteristics and relationship of the CFM and HCDM on the PRE development. The same four simulations are run again with the day-night EEJ variation, and the results are presented with gray lines in Figure 6 (to be discussed in a section below). The daytime field line-integrated profiles of the off-equator *E* regions are defined by a single 17:00 LT profile, and the nighttime profiles after 18:00 LT are the same profile divided by 20. The profiles at 18:00 LT are the average of day and nighttime profiles.

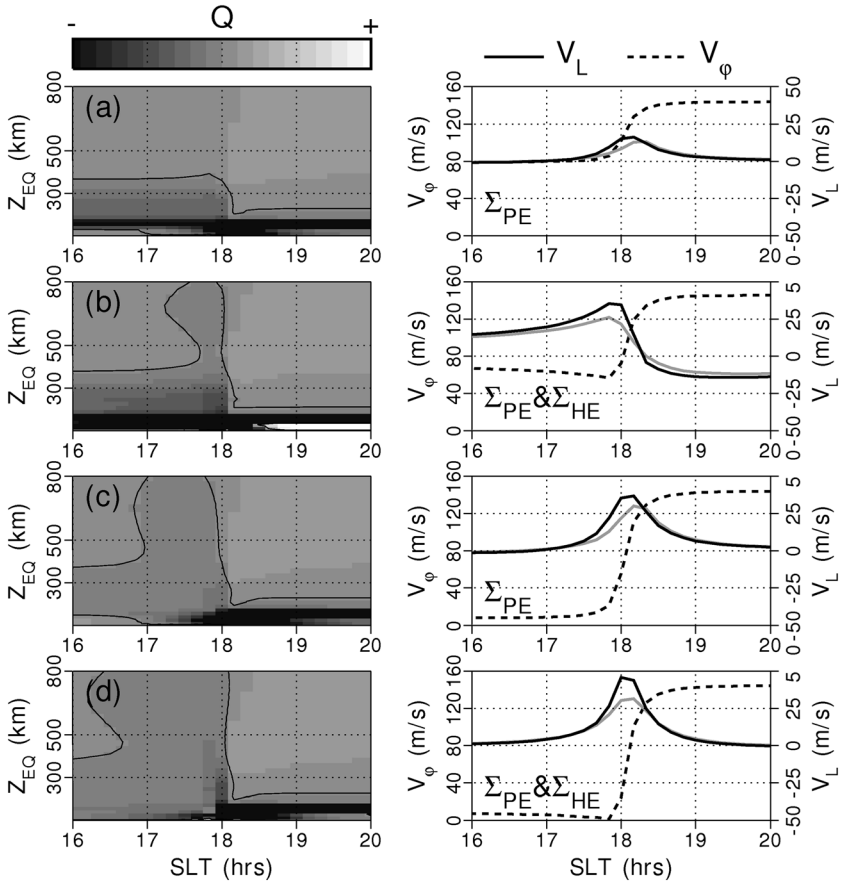

Figure 6. Simplified studies of the terminator electrodynamics. (left column) Charge density determined from a 2-D Poisson's equation with white as positive charge density and black as negative charge density with only the zero contour line. (right column) Plasma drifts at 400 km. (a) Constant eastward wind (150 m/s) with day-night differences in Σ_{PE} but no Σ_{HE} in off-equator *E* region, (b) constant eastward wind with day-night differences in Σ_{PE} and Σ_{HE}, (c) day-night differences in eastward wind and Σ_{PE} but no Σ_{HE} in off-equator *E* region, and (d) day-night differences in eastward winds Σ_{PE} and Σ_{HE}. The black lines in the right column are for nighttime EEJ conductivity values at all local times. The gray lines are for EEJ with day-night variation.

For the first two studies, we set the field line-integrated *F* region zonal wind, U_P^F, to 150 m/s for all local times (*E* region winds are zero everywhere). We also set U_P^F to zero above 2000 km to limit the *F* region dynamo region to equatorial latitudes. The 150 km apex altitude is the bottom limit of the field line-integrated *F* region. The *E*/*F* region conductivity weighting of the *F* region wind (equation (10)) above 150 km apex altitude produces a bottomside to the *F* region dynamo near 200 km, where the *F* region conductivity rapidly drops off with decreasing apex altitude due to the lack of *F* region electron density and to the decreasing length of the *F* region field line.

The first study isolates the CFM evening edge effect, which was most simply presented using the day-night variation of Pedersen-weighted zonal neutral wind (equation (10)) and the curl-free equation (equation (12)). Hall conductivity does not appear in the simple CFM derivation of the PRE presented in section 3.1. Figure 6a shows the effects of (1) the constant *F* region zonal wind, (2) a day-night variation in the *E* region Pedersen conductivity, (3) a nighttime profile of Hall conductivity in the off-equator *E* region at all local times to eliminate the HCDM effects, and (4) nighttime EEJ profiles at all local times. Figure 6a (left) plots a representative charge density on the *F* region dynamo gradients in gray scale with negative charges (darker shades) collecting on the bottomside *F* region and positive charges (lighter shades) collecting on the top of the *F* region dynamo (~1500 to 2000 km), although we do not plot up to 2000 km to preserve more detail near the *F* region bottomside. Figure 6a (right) shows the zonal drift (V_φ, dashed black line) and the vertical drift (V_L, solid black line) at 400 km. The high *E* region Pedersen conductivity during the

day reduces the vertical polarization electric field required to drive the downward Pedersen current ($\Sigma_{PE}E_L$) that balances the upward *F* region dynamo Pedersen current ($\Sigma_{PE}BU_\varphi$). The rapid change in the vertical polarization electric field at sunset produces a 20 m/s vertical plasma drift response. The negative charge density (black) on the bottomside of the *F* region has an abrupt change at sunset. There is no net charge accumulation on the terminator in between the bottomside and topside positions. The PRE of this simulation is due to the edge effect of the *F* region dynamo (CFM).

The second simulation (Figure 6b) uses (1) the constant *F* region zonal wind, (2) a day-night variation in the off-equator *E* region Pedersen and Hall conductivities, and (3) nighttime EEJ profiles at all local times. Both CFM and HCDM are present in the simulation. The HCDM is generated by gradients in the Hall currents driven in the *E* region conductivity away from the dip equator by the downward (equatorward) polarization electric field (Figure 4). Figure 6b (left) shows a terminator charge density as in the Figure 4 schematic of the HCDM but with strong focus on lower apex altitudes. In this constant *F* region zonal wind situation, the HCDM generates much larger vertical velocities for the PRE than does the CFM alone. However, the PRE peak occurs prior to *E* region sunset (18:00 LT). The weaker PRE of the CFM alone is now buried in the HCDM's downward drift after sunset. The HCDM may provide for an enhanced downward turning of the vertical drift after the PRE, which is frequently observed in the vertical drift.

We now consider a local time variation of the *F* region wind. The thermal gradient in the neutral gas momentum equation is westward after 14:00 LT, which drives the *F* region neutral wind eastward. Typically, the zonal neutral wind at the equator is slowed by ion-neutral drag during the day due to small zonal plasma drifts. When *E* region sunset arrives, the ionosphere begins drifting with the zonal neutral wind, which lessens the ion-neutral drag and permits a larger eastward acceleration of the *F* region neutral wind. We examine the effect of a neutral wind acceleration near sunset by setting the eastward zonal wind to 15 m/s in the dayside and the nightside neutral winds to 150 m/s and 82.5 m/s at the terminator (18:00 LT). The decrease in *E* region conductivity and the acceleration of the *F* region wind occur simultaneously in the studies for Figures 6c and 6d (black lines). Figure 6c has the same conductivity arrangement as Figure 6a (day and night Pedersen conductivities are represented; Hall conductivity off the dip equator has nighttime values only). The dayside charge accumulation on the *F* region bottomside is nearly gone in Figure 6c because the eastward neutral winds are much smaller. The nighttime charge density is nearly identical to Figure 6a. There is now a small amount of negative charge collecting at the terminator in response to the change in the *F* region neutral wind with respect to local time. This is not due to driven current across the terminator because all driven currents are vertical and Hall conductivity is near zero in this particular study. The CFM-generated PRE is larger with the simultaneous *F* region wind acceleration and *E* region decay (comparing Figures 6a and 6c). The PRE is larger because the variation of the vertical electric field at the sunset terminator in Figure 6c is larger than in Figure 6a. *Crain et al.* [1993] suggested the importance of the acceleration of the *F* region dynamo neutral wind in the evening electrodynamics. The PRE peak is again after *E* region sunset.

Figure 6d uses the same conductivities as Figure 6b and the same *F* region neutral wind as Figure 6c. In this case, the PRE of Figure 6d has about the same magnitude as the PRE of Figure 6c. The HCDM depends on the zonal gradient in the Hall current across the solar terminator, but the zonal gradient takes into account the simultaneous decrease in Hall conductivity and the increase in the downward electric field. The large HCDM effect observed in Figure 6b almost disappears in Figure 6d when the *F* region neutral wind acceleration occurs at sunset. Instead, the CFM effect remains with only a slight presunset increase in vertical drift generated by the HCDM. A geophysically realistic simulation of conjugate *E* region conductivities and *F* region neutral winds is needed to accurately assess the relative importance of the CFM and HCDM on PRE magnitudes. However, the HCDM will be smaller than proposed by *Farley et al.* [1986] because the constant large *F* region neutral wind across the solar terminator never occurs.

These studies suggest that the HCDM has limited influence on the PRE magnitude but does influence the presunset period of the early PRE shape. The CFM is the most likely primary cause of the PRE for simultaneous *E* region sunsets in both hemispheres. The role of the EEJ has yet to be examined.

4.2. What Is the Role of the EEJ on the PRE?

We now examine the influence of the EEJ conditions on the PRE using four simulation experiments. The four simulations in Figure 6 are repeated with the EEJ having a day-night conductivity variation with a ratio of 20

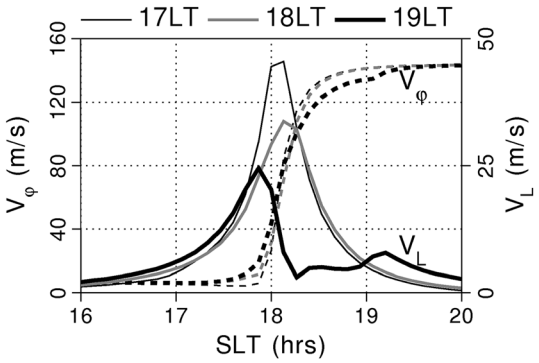

Figure 7. Different EEJ sunsets using conditions from Figure 6d. EEJ sunset centered on 17:00 LT (thin black line), 18:00 LT (gray line), and 19:00 LT (thick black line). The 18:00 LT sunset run is identical to the conditions for the gray line of Figure 6d.

to 1 and an averaged profile at the 18:00 LT node. No winds are present in the EEJ. The resulting vertical drift velocities are plotted in Figure 6 with gray lines. The zonal plasma drifts were essentially identical with the previous simulations. The four simulations show that the EEJ effectively reduces the zonal electric field generated by the unchanged electromotive force of the *F* region dynamo. For the simulations of Figures 6a and 6c where only Pedersen conductivity has day-to-night change above 150 km apex altitude, the PRE vertical drifts are reduced during the elevated daytime conductivities of the EEJ and are unchanged for the EEJ nighttime conditions. For simulations of Figure 6b when the HCDM is dominant, the elevated EEJ conductance reduces the HCDM PRE during the sunlit EEJ period. In Figure 6d where both CFM and HCDM are operating though with CFM dominance, the presence of the day-night EEJ variation reduces the PRE substantially and shifts the peak of the vertical drift to after sunset.

According to *Haerendel and Eccles* [1992], the reduction of the EEJ conductance should enhance the PRE magnitude due to the increased resistance in the path of horizontal current from the dayside ionosphere to the unbalanced upward current demand. It appears in these simulations that the EEJ is acting as merely an additional conductive path for horizontal closure, which reduces the zonal electric field magnitude required to close the unbalanced vertical current demands of the vertical current dynamo in the *F* region. The Haerendel and Eccles mechanism works in tandem with the CFM and the HCDM to generate a particular PRE magnitude and shape around sunset.

We performed a couple more simulations to examine the EEJ's role. Using the conditions of Figure 6d with CFM and HCDM both active and with the accelerating *F* region neutral wind around sunset, we performed three simulations by moving EEJ sunset to be centered on 17:00 LT, 18:00 LT, and 19:00 LT with sunset of higher apex altitudes of the off-equator *E* regions remaining centered on 18:00 LT. The results are show in Figure 7. The 17:00 LT EEJ sunset is essentially identical to the Figure 6d black line results, where EEJ is always at nighttime values. The 18:00 LT EEJ sunset is identical in conditions and results to the Figure 6d gray line results. The 19:00 LT EEJ sunset significantly modifies the sunset and postsunset plasma drifts as expected with current closure able to occur long after the 18:00 LT sunset of the dynamo currents above 150 km apex altitude. While this late EEJ sunset is unrealistic, it gives insight into the control an elevated EEJ conductivity around and after sunset will have on electric fields near sunset. This condition does arise when there is an angle between the solar terminator and the magnetic meridian. The EEJ conductivity will remain in sunlight as one of the off-equator *E* regions enters darkness. We will explore this situation in a subsequent subsection.

The decay of Hall and Pedersen conductances for the region beyond the EEJ and the decay of the EEJ Cowling conductance were both based on a day-to-night factor of 20. If the nighttime reduction of the EEJ is different than the off-equator reduction at sunset, then one can obtain a variation in the postsunset PRE magnitude. Figure 8 plots the PRE values for different day-to-night factors in the EEJ for the same conditions beyond the EEJ. The off-equator reduction is held at a divisor of 20. The EEJ sunset is centered on 18:00 LT for all three simulations but with day-to-night conductivity ratios of 10 (thin black line), 20 (gray), and 40 (thick black line). The results in Figure 8 demonstrate that EEJ conductances after sunset affect the PRE magnitude as *Haerendel and Eccles* [1992] describe. They proposed that the vertical plasma drift of the PRE can lift ionization out of the EEJ region and reduce EEJ conductance to provide a feedback increase of the PRE magnitude.

4.3. Different Altitude Profiles of CFM and HCDM

There are local time differences in the vertical plasma drifts generated by the CFM and HCDM as demonstrated in Figures 6a and 6b. The CFM PRE peak occurs at the end of sunset and is only a positive vertical drift feature. The downward drift after sunset depends on meridional neutral winds, *F* region

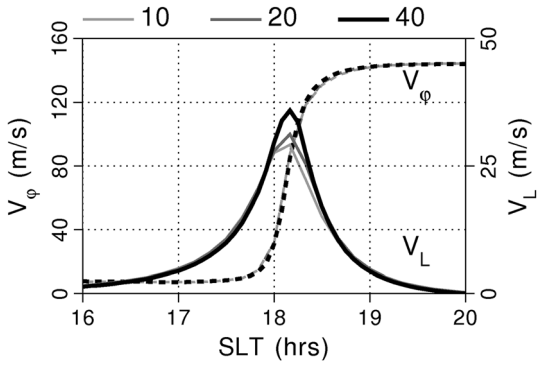

Figure 8. EEJ studies using conditions from Figure 6d outside the EEJ region. All EEJ sunsets are centered on 18:00 LT, but with day-to-night conductivity ratios are 10 (thin black line), 20 (gray line), and 40 (thick black line).

winds, and/or *E* region winds entering into the electrodynamics. The HCDM PRE peak occurs prior to sunset and generates vertical drifts away from the terminator—upward prior to sunset and downward after sunset. Another difference between the two mechanisms can be seen in the altitude profiles of the vertical drift at the peak of each PRE (Figure 9). The CFM-generated PRE vertical plasma drift decays with altitude above the bottomside of the *F* region dynamo (solid lines). We must note that the CFM vertical drift profile below 300 km is suspect in this simulation since the *F* region profile used has a 17:00 LT profile and its electron density profile is much too low after sunset. However, the topside falloff of vertical drift of the PRE during equinox conditions was observed in averaged San Marco satellite data (Figure 6 of *Eccles et al.* [1999]). The topside decay of the PRE associated with the curl-free CFM was calculated by *Eccles* [1999a] and recently measured by *Fejer et al.* [2014]. The HCDM depends on a current gradient source term distributed along the solar terminator in the off-equator Hall conductivity, that is, distributed in apex altitude in the field line-integrated model. One might expect the altitude of the HCDM PRE to have a slower falloff with apex altitude, which is the case (Figure 9, dashed lines). The influence of the EEJ conductance affects the PRE magnitudes of both mechanisms but not the altitude profiles above the *F* region bottomside. Figure 9 black lines are from Figures 6a and 6b where the nighttime profiles of the EEJ are used for all local times. The gray lines plot the altitude profiles of the PRE peaks from Figures 6c and 6d where the EEJ has the day-night conductivity ratio of 20.

4.4. Equinox and Solstice Sunset Conditions in the Off-Equator *E* Regions

Tsunoda [1985] presented evidence that the equatorial spread *F* occurrence rate is controlled by the longitudinal gradient of the *E* region Pedersen conductivity of the combined hemispheres. The sunset gradient of the total field line-integrated conductivity changes with the seasonal variation of the solar terminators with respect to the declination of the magnetic meridian. It can be suggested that the PRE magnitude also holds a proportional relationship with the speed of the combined *E* region sunsets of each hemisphere (equations (10) and (12)). The slower sunset decay of the *E* region conductivity when the terminator is not aligned with the magnetic meridian might reduce the CFM-caused PRE, which, in turn, permits a low *F* region bottomside after sunset and increased collisional stability.

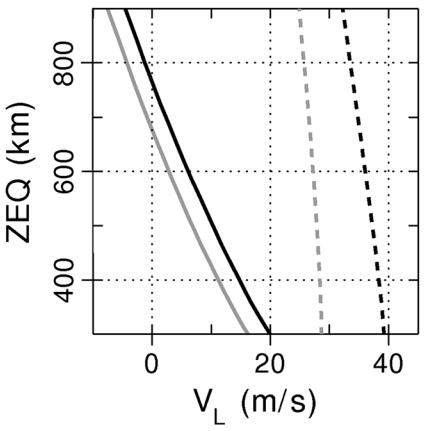

Figure 9. Altitude profile of vertical drift for the CFM PRE maximum for the conditions in Figure 6a at 18:10 LT (solid line) and the HCDM PRE maximum for the conditions in Figure 6b at 17:50 LT (dash line). The black lines are for EEJ conductivities at nighttime values for all local times. The gray lines are for runs with day-night variation within EEJ.

We now examine the effect of offsetting the sunsets of the northern and southern hemisphere *E* regions on the CFM, HCDM, and the role of the EEJ mechanisms for the PRE. We increase the spatial resolution of the simulations to 1.25° longitude (5 min local time) to better resolve the PRE peaks. The day-to-night ratio of all *E* region Pedersen and Hall conductivity profiles is 20. Sunset in each hemisphere is modeled with a linear decay in the *E* region over a 30 min period. For reference, we first examine simultaneous *E* region sunsets from 17:45 LT to 18:15 LT at all apex altitudes, that is, for *E* regions of both hemispheres and the EEJ region. The *F* region conductivity profile remains constant for all local times to simulate the much slower decrease in *F* region conductivity.

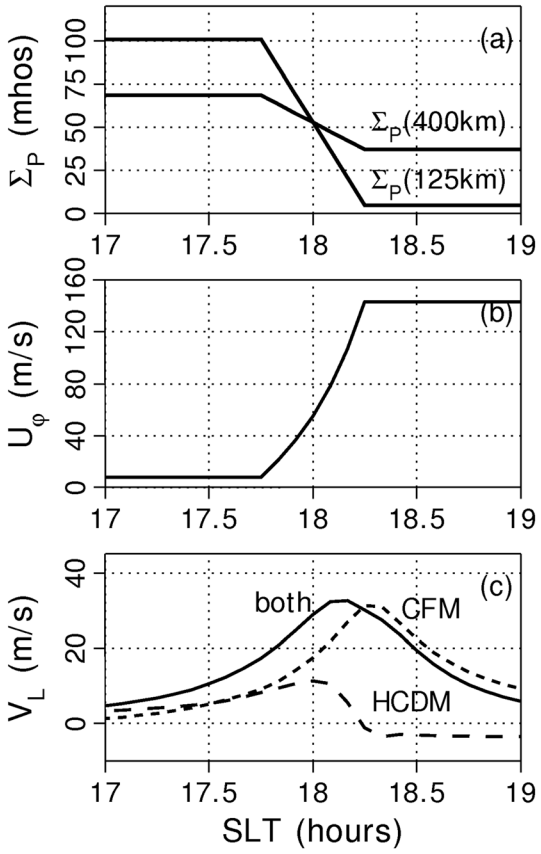

Figure 10. Runs results for equinox-aligned sunset from 17:45 LT to 18:15 LT. (a) Field line-integrated Pedersen conductance at 400 km and 125 km apex altitudes, (b) Pedersen-weighted zonal neutral wind, and (c) vertical plasma drift at 400 km apex altitude with CFM (short dash) and HCDM (long dash) components plotted.

Figure 10a plots the field line-integrated Pedersen conductance at 400 km apex altitude near the *F* region peak (includes *F* region and both *E* regions) and at 125 km altitude near the peak of Pedersen conductivity in the EEJ. The *F* region wind linearly increases from 15 m/s prior to sunset to 150 m/s post during the 0.5 h sunset period. Figure 10b plots the conductivity-weighted zonal neutral wind, which weights the linear *F* region wind with the zero winds of the *E* region. The current continuity equation is solved to obtain the electric potential, electric fields, and the plasma drifts as with earlier simulations. Figure 10c presents the results of two simulations and their differences. The first simulation held the off-equator Hall conductivity to nighttime levels through all local times to highlight the CFM (short dashed line in Figure 10c). The second used full day-night variation of both Hall and Pedersen conductivities for the PRE solution with CFM and HCDM operating (solid line in Figure 10c). These two solutions are differenced to obtain the HCDM effect in isolation (long dashed line in Figure 10c). The CFM dominates the PRE magnitude, but the HCDM moves the PRE to early local times prior to the complete *E* region sunset of 18:15 LT. This result generally agrees with the sharp terminator of the earlier studies.

We now simulate solstice conditions with the center of the 0.5 h sunset period varying with apex altitude (field line-connected *E* region longitude). The EEJ sunset still is centered on 18:00 LT and occurs between 17:45 LT and 18:15 LT. For these northern winter solstice conditions, the northern and southern *E* region sunsets connected to the *F* region peak at about 400 km are fully separated in time. This can be seen in the three tiers in the Pedersen conductivity at 400 km apex altitude (Figure 11a). The middle tier occurs because the northern *E* region sunset is complete and the southern *E* region hemisphere sunset has not yet begun for the 400 km apex altitude. For this study, the *F* region zonal neutral wind is assumed to accelerate linearly between the initiation of northern hemisphere *E* region sunset near 17:20 LT and the final moment of the southern hemisphere *E* region sunset near 18:40 LT (Figure 11b). This slower acceleration assumes a slowly decreasing ion-neutral drag term on the neutral wind. With the slower acceleration of the zonal neutral wind and the slower decay of the combined *E* region conductivities, one would expect a reduced PRE magnitude. However, the PRE peak drift produced in this solstice simulation (Figure 11) is larger and later than the equinox case (Figure 10), $V_L = 43$ m/s, $t_{peak} = 18{:}25$ LT, and $V_L = 33$ m/s, $t_{peak} = 18{:}10$ LT, respectively.

In the solstice condition, the CFM PRE component is reduced from 30 m/s to ~25 m/s in the equinox case and is moved from 18:20 LT to 18:35 LT. The solstice CFM PRE is timed with the southern hemisphere decay of conductivity. The time-rate-of-change of the equinox conductivity should be twice the time-rate-of-change of the southern hemisphere conductivity. Additionally, there is a reduced acceleration for the zonal wind, so one would expect the solstice CFM PRE component to be less than one half of the equinox CFM PRE. However, the EEJ has experienced its full sunset at 18:15 LT, so the combined rate-of-change of the southern hemisphere conductivity change and the wind acceleration is permitted a sizable CFM PRE.

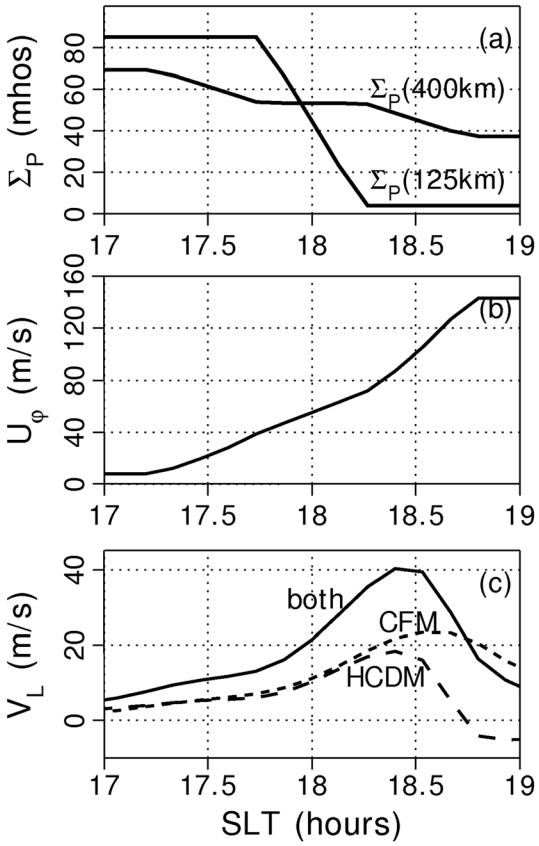

Figure 11. Runs results for solstice conditions of unaligned sunsets. (a) Field line-integrated Pedersen conductance at 400 km and 125 km apex altitudes, (b) Pedersen-weighted zonal neutral wind, and (c) vertical plasma drift at 400 km apex altitude with CFM (short dash) and HCDM (long dash) components plotted.

The HCDM component of the PRE is now twice as large for the solstice conditions over the equinox conditions. The peak of the HCDM mechanism occurs at the EEJ sunset of 18:15 LT. Unlike the equinox situation, there is still a sunlit portion of the southern *E* region with elevated Hall conductivity after the EEJ sunset. Thus, the HCDM mechanism can participate in the PRE magnitude determination during solstice conditions.

The solstice situation demonstrates the complex relationships of the CFM and HCDM with the EEJ sunset in determining the enhancement of the vertical plasma drift near sunset. The sunlit EEJ region reduces the CFM and HCDM effects on PRE electric fields, but the CFM and HCDM effects are magnified once the EEJ region enters darkness and their processes continue due to the sunlit southern hemisphere for northern winter solstice. During equinox-type conditions, the EEJ remains sunlit during the period that the HCDM is in effect, thus reducing its importance. A more realistic assessment of these mechanisms must be performed using coupled ionosphere-thermosphere-electrodynamic models to properly assess the variation of the PRE through seasonal changes and geographic sectors.

5. Discussion and Conclusion

Three mechanisms have been proposed for the generation of the prereversal enhancement (PRE) of the vertical plasma drift (zonal electric field) in the equatorial ionosphere. We examined these mechanisms using the field line-integrated electrodynamic description. All are dependent on the *F* region dynamo action around the rapidly changing conditions near the sunset terminator. The first causal mechanism was proposed in a single sentence by *Rishbeth* [1971b] and was later discussed in detail by *Eccles* [1998a], that is, an edge effect or curl-free mechanism (CFM) which generates a positive zonal electric field and upward plasma drift that is proportional to the rapid change at *E* region sunset in the downward polarization electric field generated by the *F* region neutral wind dynamo. The peak of the PRE generated by the CFM generally occurs at the end of the *E* region sunset of the combined hemispheres. The second mechanism is the Hall current divergence mechanism (HCDM) proposed by *Farley et al.* [1986], which depends on the downward electric fields generated by the *F* region dynamo. However, the downward electric of the *F* region dynamo field must be present prior to sunset to drive zonal Hall currents toward the *E* region sunset boundary in the off-equator Hall conductivity. As the Hall conductance decays, a current divergence arises creating a source term for an eastward electric field before sunset and a westward electric field after sunset. As a result, an HCDM PRE peak would occur just prior to the off-equator *E* region sunset. The third mechanism or influence on the PRE is associated with the decay of the conductivity in the equatorial Cowling conductivity or the equatorial electrojet (EEJ) region. *Haerendel and Eccles* [1992] proposed that the conductivity decay of this region during sunset elevates the zonal electric fields (vertical drift) required to meet current continuity requirements of the rapidly changing *F* region dynamo electrodynamics near sunset. We demonstrate that the sunlit EEJ role is the key moderating current load near the solar terminator. The sunlit EEJ reduces zonal electric fields being generated by the CFM and HCDM. After EEJ region sunset, the CFM and HCDM are able to produce larger PRE fields. The PRE's magnitude and local time location are governed by EEJ region sunset, while the generative sources of the PRE are found in the

CFM and HCDM as a result of the *F* region dynamo near sunset. There is a slight effect of the EEJ on the PRE magnitude after EEJ sunset as suggested by *Haerendel and Eccles* [1992] depending on the degree of conductivity reduction occurring from day-to-night ionization processes as well as dynamic influences.

We examine the equinox case and demonstrate that the CFM dominates the generation of the PRE peak magnitude. Due to the daytime ion-neutral drag on the *F* region zonal wind, the daytime downward electric field generated by the *F* region dynamo is small, and the acceleration of the wind happens as the *E* region sunset progresses. *Farley et al.* [1986] used a constant zonal *F* region wind across the terminator to produce a large PRE resulting from the HCDM. Our simulations show that when the constant neutral wind is replaced with an accelerating neutral wind around sunset, the influence of the HCDM on the PRE is greatly reduced. The HCDM has only a small influence on the CFM-generated PRE when the sunset terminator and the magnetic meridian are aligned. The positive gradient in the eastward *F* region dynamo wind increases the CFM influence and decreases the HCDM influence on the PRE.

The simulations revealed that the PRE produced by the CFM and the HCDM have peaks at different times in relationship to the solar sunset in the off-equator *E* region. The HCDM PRE would be before sunset, and the CFM PRE is at the end of sunset. Additionally, the altitude profiles of the CFM and the HCDM differ. The HCDM PRE profiles vary only slightly with altitude, while the CFM PRE profile decays with altitude above the bottomside of the *F* region. We also examine the relationship of the CFM, the HCDM, and the role of the EEJ region during solstice conditions when the off-equator *E* region sunsets differ. In the northern winter solstice simulation, the northern hemisphere *E* region sunset occurred prior to the EEJ sunset, which occurred prior to the southern hemisphere *E* region sunset. The northern *E* region sunset has little effect on the magnitude of the PRE because the EEJ region is still sunlit and reduces any zonal electric field generated by the HCDM and CFM. The acceleration of the *F* region zonal wind during the extended integrated sunset period permits the generation of downward polarization electric fields while the southern hemisphere *E* region is still sunlit. This permits the HCDM to become an important influence on the PRE prior *E* region darkness in the south after EEJ sunset. The CFM effect maximizes just at the end of the southern hemisphere sunset. The combined CFM and HCDM during solstice produced a larger PRE than the equinox condition in this simplified study. Typically, the equinox condition is thought to be more suitable for a larger PRE associated with the CFM. Indeed, the CFM component was smaller for the solstice case, but the combined CFM and HCDM components produced a larger PRE herein. There are many factors in a realistic solstice run that might further reduce the PRE magnitude, but they are probably due to other effects not examined within these simplified simulations. For example, the meridional wind system is important near sunset during solstice, and the meridional winds can move *F* region ionization upward in one hemisphere and downward in the other. The conductivity-weighted neutral wind dynamo driving the PRE electrodynamics may be substantially less under these conditions. Also, the *E* region tides and *F* region meridian wind may also reduce the PRE during the solstice condition.

The PRE can be more fully modeled with coupled models of the ionosphere, thermosphere, and electric field. Models must have proper magnetic conjugate coupling of the *E* regions to capture seasonal and geographic variations. The coupled ionosphere and thermosphere must accommodate the changing ion drag characteristics on the acceleration of the *F* region zonal wind as well as the adjustment of *F* region plasma by meridonal winds. Finally, a reasonable model for the conductivity of the EEJ region is required to properly model its moderating influence. All of these will appropriately activate the electrodynamics of the PRE magnitude and time with the curl-free response, the Hall current divergence, the acceleration of the zonal neutral wind in the *F* region, and the participation of the EEJ as a regulating current path.

Appendix A

The 3-D Gauss' law for the electric field can be reduced to a 2-D equation under the assumption of infinite parallel conductivity. This usefully provides an indicator of the charging of field lines in the ionosphere when using 2-D field line-integrated electrodynamics [*Haerendel*, 1973; *Haerendel et al.*, 1992]. The local dipole coordinate (*l*, *q*, and *s*) system is defined as follows: $\hat{\mathbf{l}}$ is the unit vector along **B**, $\hat{\mathbf{q}}$ is transverse to **B** in the meridional plane (+upward), and $\hat{\mathbf{s}}$ is transverse to **B** (zonal horizontal vector) with $\hat{\mathbf{s}}=\hat{\mathbf{l}}\times\hat{\mathbf{q}}$. The polar coordinate system (L,φ) is in the magnetic equatorial plane. L is the radius of the apex of the dipole field

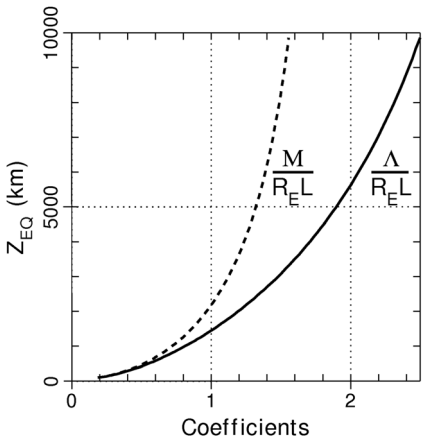

Figure 12. Coefficients of the 2-D Poisson's equation for infinitely conducting dipole field lines.

line measured in Earth radii, R_E, and φ is the eastward longitude in degrees. The radius along the field line is related to the apex radius by the formula

$$r = R_E L\left(1-\zeta^2\right) \tag{A1}$$

where $\zeta = \sin\lambda$ with λ as the magnetic latitude. The differentials are given by

$$dl = \left(1+3\zeta^2\right)^{\frac{1}{2}} R_E L d\zeta \tag{A2}$$

$$dq = \frac{\left(1-\zeta^2\right)^{\frac{3}{2}}}{\left(1+3\zeta^2\right)^{\frac{1}{2}}} R_E dL \tag{A3}$$

$$ds = \left(1-\zeta^2\right)^{\frac{3}{2}} R_E L d\varphi \tag{A4}$$

The local divergence of the electric field is given by

$$\nabla\cdot\mathbf{E} = \frac{\partial E_q}{\partial q} + \frac{\partial E_s}{\partial s} + \frac{\partial E_l}{\partial l} = \frac{\rho}{\varepsilon_o} \tag{A5}$$

With the assumption of a very large parallel conductivity, E_l goes to zero along the field line, and the charge distributes suitably along the field line. The perpendicular electric field components along the field line are related to the values at the apex of the line through

$$E_s = E_\varphi \frac{1}{\left(1-\zeta^2\right)^{\frac{3}{2}}} \tag{A6}$$

$$E_q = E_L \frac{\left(1+3\zeta^2\right)^{\frac{1}{2}}}{\left(1-\zeta^2\right)^{\frac{3}{2}}} \tag{A7}$$

where E_L and E_φ are the functions of L and φ. Multiplying both sides of equation (A5) by a unit volume $dqdsdl$ and integrating along l from the bottom of the E region in the southern hemisphere to below the E region in the north captures the total charge collected on the field line.

$$\int_{l_S}^{l_N}\left(\frac{\partial E_q}{\partial_q} + \frac{\partial E_S}{\partial_S}\right) dqdsdl = \int_{l_S}^{l_N} \frac{\rho}{\varepsilon_o} dqdsdl \tag{A8}$$

We move from q, s, and l to L, φ, and ζ for the integration along field lines and divide by the differential area of the 2-D coordinate system to obtain the 2-D charge density definition below. The differentials (equations (A2)–(A4)) and the electric field relations used to obtain relations for magnetic local and apex polar coordinate system through partial differential chain rule give

$$\frac{\partial E_q}{\partial q} = \frac{\left(1+3\zeta^2\right)}{\left(1-\zeta^2\right)^3} \frac{1}{R_E L} \frac{\partial L E_L}{\partial L} \tag{A9}$$

$$\frac{\partial E_s}{\partial s} = \frac{1}{\left(1-\zeta^2\right)^3} \frac{1}{R_E L} \frac{\partial E_\varphi}{\partial \varphi} \tag{A10}$$

These relations with the differential relation in equation (A2) give

$$\frac{1}{R_E L}\left(\Lambda(L)\frac{\partial L E_L}{\partial L} + \mathrm{M}(L)\frac{\partial E_\varphi}{\partial \varphi}\right) = \frac{Q}{\varepsilon_o} \tag{A11}$$

where the coefficients and integrated charge are defined as

$$\Lambda(L) = R_E L \int_{\zeta_S(L)}^{\zeta_N(L)} \left(1+3\zeta^2\right)\partial\zeta \tag{A12}$$

$$M(L) = R_E L \int_{\zeta_S(L)}^{\zeta_N(L)} \partial\zeta \tag{A13}$$

$$Q(L,\varphi) = R_E L \int_{\zeta_S(L)}^{\zeta_N(L)} \rho\left(1-\zeta^2\right)^3 d\zeta \tag{A14}$$

The limits of the integrations are determined through equation (A1) using an altitude below the *E* region conductivity (70 km in this paper). *Q* is the field line-integrated charge density within the two-dimensional differential volume $R_E^2 L\ dL\ d\varphi$. The coefficients in the divergence of the electric field result from the distribution of the charge along the dipole field lines due to infinite parallel conductivity (Figure 12). This is the equation used to relate charge distribution on field lines with the solution of a 2-D current continuity model.

Acknowledgments
Data from model simulations within this article are available at www.spacenv.com/publications/eccles/JGR_PRE1/index.html. The ionosphere model is an SEC proprietary model. This work was in part supported by the National Science Foundation under grant ATM0745714 and personal time. J.P. St. Maurice thanks the Canada Research Chair program at the University of Saskatchewan for supporting his contributions to this work.

Alan Rodger thanks the reviewer for the assistance in evaluating this paper.

References

Baker, W. G., and D. F. Martyn (1953), Electric currents in the ionosphere—The conductivity, *Philos. Trans. R. Soc. London, Ser. A*, *246*, 281–320.
Chapagain, N. P., D. J. Fisher, J. W. Meriwether, J. L. Chau, and J. J. Makela (2013), Comparison of zonal neutral winds with equatorial plasma bubble and plasma drift velocities, *J. Geophys. Res. Space Physics*, *118*, 1802–1812, doi:10.1002/jgra.50238.
Crain, D., R. Heelis, G. Bailey, and A. Richmond (1993), Low-latitude plasma drifts from a simulation of the global atmospheric dynamo, *J. Geophys. Res.*, *98*, 6039–6046, doi:10.1029/92JA02196.
Drob, D. P., et al. (2008), An empirical model of the Earth's horizontal wind fields: HWM07, *J. Geophys. Res.*, *113*, A12304, doi:10.1029/2008JA013668.
Eccles, J. V. (1998a), A simple model of low-latitude electric fields, *J. Geophys. Res.*, *103*, 26,699–26,708, doi:10.1029/98JA02657.
Eccles, J. V. (1998b), Modeling investigation of the evening pre-reversal enhancement of the zonal electric field in the equatorial ionosphere, *J. Geophys. Res.*, *103*, 26,709–26,719, doi:10.1029/98JA02656.
Eccles, J. V. (2004), The effect of gravity and pressure in the electrodynamics of the low-latitude ionosphere, *J. Geophys. Res.*, *109*, A05304, doi:10.1029/2003JA010023.
Eccles, J. V., N. Maynard, and G. Wilson (1999), Study of the evening plasma drift vortex in the low-latitude ionosphere using San Marco electric field measurements, *J. Geophys. Res.*, *104*, 28,133–28,143, doi:10.1029/1999JA900373.
Eccles, V., D. D. Rice, J. J. Sojka, C. E. Valladares, T. Bullett, and J. L. Chau (2011), Lunar atmospheric tidal effects in the plasma drifts observed by the Low-Latitude Ionospheric Sensor Network, *J. Geophys. Res.*, *116*, A07309, doi:10.1029/2010JA016282.
Farley, D. T., Jr. (1959), A theory of electrostatic fields in a horizontally stratified ionosphere subject to a vertical magnetic field, *J. Geophys. Res.*, *64*, 1225–1233, doi:10.1029/JZ064i009p01225.
Farley, D. T., E. Bonelli, B. G. Fejer, and M. F. Larsen (1986), The pre-reversal enhancement of the zonal electric field in the equatorial ionosphere, *J. Geophys. Res.*, *91*, 13,723–13,728, doi:10.1029/JA091A112p13723.
Fejer, B. G., E. Kudeki, and D. T. Farley (1985), Equatorial *F* region zonal plasma drifts, *J. Geophys. Res.*, *90*, 12,249–12,255, doi:10.1029/JA090iA12p12249.
Fejer, B. G., L. Scherliess, and E. R. de Paula (1999), Effects of the vertical plasma drift velocity on the generation and evolution of equatorial spread *F*, *J. Geophys. Res.*, *104*, 19,859–19,869, doi:10.1029/1999JA900271.
Fejer, B. G., J. R. Souza, A. S. Santos, and A. E. C. Perreira (2005), Climatology of *F* region zonal drifts over Jicamarca, *J. Geophys. Res.*, *110*, A12310, doi:10.1029/2005JA011324.
Fejer, B. G., D. Hui, J. L. Chau, and E. Kudeki (2014), Altitudinal dependence of evening equatorial *F* region vertical plasma drifts, *J. Geophys. Res. Space Physics*, *119*, 5877–5890, doi:10.1002/2014JA019949.
Finley, C. C., et al. (2010), International Geomagnetic Reference Field: The eleventh generation, *Geophys. J. Int.*, *183*, 1216–1230.
Forbes, J. M., and R. S. Lindzen (1976), Atmospheric solar tides and their electrodynamic effects. Part I. The global *Sq* current system, *J. Atmos. Terr. Phys.*, *38*, 897–910.
Haerendel, G. (1973), Theory of equatorial spread *F*, preprint Max-Planck-Instit. für extraterr. Phys., Garching bei Munchen, Germany.
Haerendel, G., and J. V. Eccles (1992), The role of the equatorial electrojet in the evening ionosphere, *J. Geophys. Res.*, *97*, 1181–1192, doi:10.1029/91JA02227.
Haerendel, G., J. V. Eccles, and S. Çakir (1992), Theory for modeling the equatorial evening ionosphere and the origin of the shear in the horizontal plasma flow, *J. Geophys. Res.*, *97*, 1209–1223, doi:10.1029/91JA02226.
Heelis, R. A., P. C. Kendall, R. J. Moffett, D. W. Windle, and H. Rishbeth (1974), Electrical coupling of the *E* and *F*-regions and its effect on *F*-region drifts and winds, *Planet. Space Sci.*, *22*, 743–756.
Huba, J. D., G. Joyce, and J. Krall (2008), Three-dimensional equatorial spread *F* modeling, *Geophys. Res. Lett.*, *35*, L10102, doi:10.1029/2008GL033509.
Kudeki, E., B. G. Fejer, D. T. Farley, and H. M. Ieric (1981), Interferometric studies of equatorial *F* region irregularities and drifts, *Geophys. Res. Lett.*, *8*, 377–380, doi:10.1029/GL008i004p00377.
Picone, J. M., A. E. Hedin, D. P. Drob, and A. C. Aikin (2002), NRLMSISE-00 empirical model of the atmosphere: Statistical comparisons and scientific issues, *J. Geophys. Res.*, *107*(A12), 1468, doi:10.1029/2002JA009430.
Prakash, S., D. Pallamraju, and H. S. S. Sinha (2009), Role of the equatorial ionization anomaly in the development of the evening pre-reversal enhancement of the equatorial zonal electric field, *J. Geophys. Res.*, *114*, A02301, doi:10.1029/2007JA012808.
Richmond, A. D., and T.-W. Fang (2015), Electrodynamics of the equatorial evening ionosphere: 2. Conductivity influences on convection, current, and electrodynamic energy flow, *J. Geophys. Res. Space Physics*, *120*, 2133–2147, doi:10.1002/2014JA020935.
Richmond, A. D., S. Matsushita, and J. D. Tarpley (1976), On the production mechanism of electric currents and fields in the ionosphere, *J. Geophys. Res.*, *81*, 547–555, doi:10.1029/JA081i004p00547.
Rishbeth, H. (1971a), The *F*-layer dynamo, *Planet. Space Sci.*, *19*, 263–267.
Rishbeth, H. (1971b), Polarization fields produced by winds in the equatorial F-region, *Planet. Space Sci.*, *19*, 357–369.
Rishbeth, H. (1973), Further studies of directional *F*-layer currents, *Planet. Space Sci.*, *19*, 357–369.
Scherliess, L., and B. G. Fejer (1998), Satellite studies of mid- and low-latitude ionospheric disturbance zonal plasma drifts, *Geosphys. Res. Lett.*, *25*, 1503–1506, doi:10.1029/98GL01032.
Scherliess, L., and B. Fejer (1999), Radar and satellite global equatorial *F* region vertical drift model, *J. Geophys. Res.*, *104*, 6829–6842, doi:10.1029/1999JA900025.
Schunk, R. W., J. J. Sojka, and J. V. Eccles (1997), Expanded capabilities for the ionospheric forecast model *Rep. AFRL-VS-HA-TR-98-0001*, Air Force Res. Lab., Space Vehicles Direct., Hanscom, Mass.
Singh, A., and K. D. Cole (1987a), A numerical model of the ionospheric dynamo—I. Formulation and numerical technique, *J. Atmos. Terr. Phys.*, *49*, 521–527.

Singh, A., and K. D. Cole (1987b), A numerical model of the ionospheric dynamo—II. Electrostatic field at equatorial and low latitudes, *J. Atmos. Terr. Phys.*, *49*, 529–537.

Singh, A., and K. D. Cole (1987c), A numerical model of the ionospheric dynamo—III. Electric current at equatorial and low latitudes, *J. Atmos. Terr. Phys.*, *49*, 539–547.

Stening, R. J. (1969), An assessment of the contributions of various tidal winds to the *Sq* current system, *Planet. Space Sci.*, *17*, 889–908.

Tarpley, J. D. (1970a), The ionospheric wind dynamo—I. Lunar tides, *Planet. Space Sci.*, *18*, 1075–1090.

Tarpley, J. D. (1970b), The ionospheric wind dynamo—II. Solar tides, *Planet. Space Sci.*, *18*, 1091–1103.

Titheridge, J. E. (1998), Temperatures in the upper ionosphere and plasmasphere, *J. Geophys. Res.*, *103*, 2261–2277, doi:10.1029/97JA03031.

Tsunoda, R. T. (1985), Control of the seasonal and longitudinal occurrence of equatorial scintillations by the longitudinal gradient in integrated *E* region Pedersen conductivity, *J. Geophys. Res.*, *90*, 447, doi:10.1029/JA090iA01p00447.

Tsunoda, R. T., R. C. Livingstone, and C. L. Rino (1981), Evidence of a velocity shear in bulk plasma motion associated with the post-sunset rise of the equatorial *F* layer, *Geophys. Res. Lett.*, *8*, 807–810, doi:10.1029/GL008i007p00807.

Woodman, R. F., and C. La Hoz (1976), Radar observations of *F* region equatorial irregularities, *J. Geophys. Res.*, *81*, 5447–5466, doi:10.1029/JA081i031p05447.